Dalton Transactions

ROYAL SOCIETY OF CHEMISTRY

PAPER

View Article Online
View Journal | View Issue

Cite this: *Dalton Trans.*, 2026, **55**, 6407

In or out? Adaptive metal binding by a diphosphine-based Zr metal–organic cage

Jiehye Shin and Casey R. Wade *

A lantern-type Zr metal–organic cage (MOC), **Zr–P_2N_2**, has been synthesized using ditopic carboxylate linkers based on the 1,5-diaza-3,7-diphosphacyclooctane (P_2N_2) ligand platform. Single-crystal X-ray diffraction shows that the diphosphine groups of the P_2N_2 linkers point into the confined MOC cavity. Postsynthetic metalation of the diphosphine groups with Pd and Pt precursors generates the heterobimetallic cages **Zr–P_2N_2–$PdCl_2$** and **Zr–P_2N_2–$PtCl_2$**. Structural characterization reveals that the linkers flip to accommodate metal chelation, resulting in outward facing metal diphosphine groups. Conversely, reaction of **Zr–P_2N_2** with $AgPF_6$ results in formation of **Zr–P_2N_2–Ag**, containing a hexasilver core supported by phosphine complexation within the cage interior. This work highlights the adaptive structural behavior of **Zr–P_2N_2** which provides new opportunities for designing responsive MOCs.

Received 4th March 2026,
Accepted 30th March 2026

DOI: 10.1039/d6dt00536e

rsc.li/dalton

Introduction

Metal–organic cages (MOCs) have attracted increasing interest for applications in catalysis and molecular separation owing to their chemical tunability and inherent porosity.[1–3] MOCs are considered molecular analogues of metal–organic frameworks (MOFs).[4] Both are assembled from organic linkers and metal ions or clusters and exhibit well-defined cavities or pores. However, unlike MOFs, the molecular nature of MOCs confers solubility and solution-state processability, providing unique opportunities for heterogeneous and homogeneous catalyst design.[5]

A common strategy for designing MOC-based catalysts involves using linkers with secondary ligand groups for catalytic metal binding.[6–8] Hard–soft acid–base principles are often exploited to impart orthogonal reactivity between the primary donor groups necessary for cage self-assembly and the secondary ligand groups. For example, the combination of hard Lewis acidic metal ions such as Zr^{4+} with hard carboxylate ligands can facilitate cage assembly while softer Lewis basic ligands remain available for catalyst binding. Catalytically active metal fragments can be selectively complexed at the secondary donor sites, either *via* postsynthetic reactions or cage assembly with metallolinkers.[9,10] This general strategy has been used to design a variety of heterometallic MOCs with nitrogen-based secondary ligand groups such as bipyridines.[11–14]

Phosphine ligands are widely used in homogeneous catalysis owing to their steric and electronic versatility and ability to support catalytically active late transition metal species.[15–18] However, there have been relatively few reports of MOCs containing phosphines as secondary ligand groups. Nitschke and co-workers reported a Zn-based MOC (Scheme 1A) assembled from triarylphosphine-based linkers.[19] The phosphine groups were found to react with $AuCl(SMe_2)$, resulting in binding of four AuCl units at the exterior of the tetrahedral cage. Surprisingly, the phosphine MOC exhibited no reaction with other late transition metal precursors such as $[Pd(MeCN)_4](BF_4)_2$ and $[Cu(MeCN)_4]OTf$. More recently, Cui, Liu, and co-workers reported the synthesis of a tetrahedral Zr MOC (Scheme 1B) using linkers based on chiral 2,2′-bis(diphenylphosphino)-1,1′-binaphthyl (BINAP) ligands.[20] The BINAP groups were metalated with CuOTf and $NiCl_2$ to generate heterometallic MOCs that catalyze asymmetric alkylation and alkynyl amination reactions as homogeneous catalysts.

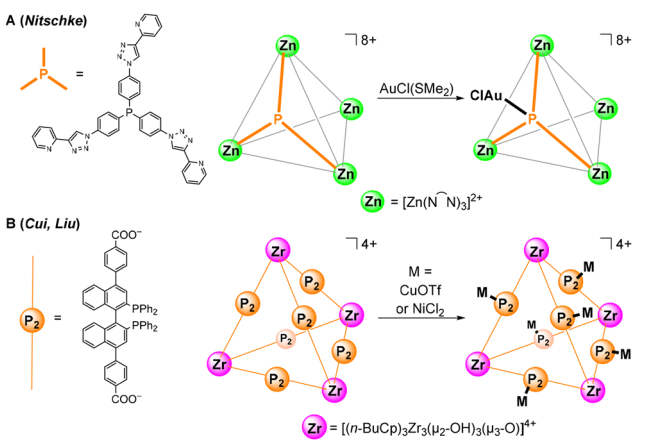

Scheme 1 Reported MOCs with phosphine-containing linkers.

Department of Chemistry and Biochemistry, The Ohio State University, 100 West 18th Ave, Columbus, OH 43210, USA. E-mail: wade.521@osu.edu

Herein, we describe the synthesis and characterization of a novel, lantern-type Zr MOC, **Zr–P_2N_2**, assembled from diphosphine-based linkers (Scheme 2). The ditopic linkers are based on the 1,5-diaza-3,7-diphosphacyclooctane (P_2N_2) ligand platform, which has been widely studied in homogeneous catalyst design.[21–23] The new MOC undergoes postsynthetic metalation with $PdCl_2$(cod), $PtCl_2$(cod), and $AgPF_6$, revealing that metal chelation at the diphosphine sites requires marked structural changes including an outward flip of the linker groups.

Results and discussion

Synthesis and characterization of Zr–P_2N_2

The $H_2(P_2N_2)$ linker was synthesized following a reported procedure.[24] **Zr–P_2N_2** was obtained as colourless crystals by solvothermal reaction of $H_2(P_2N_2)$ with Cp_2ZrCl_2 in a *N*,*N*-diethylformamide (DEF) and H_2O solvent mixture (Scheme 2). Single crystal X-ray diffraction (SCXRD) revealed formation of a lantern-type cage comprised of a pair of $[(CpZr)_3(OH)_3O]^{4+}$ clusters bridged by three $(P_2N_2)^{2-}$ linkers (Fig. 1a, Table S1). The 8-membered P_2N_2 heterocycle adopts a crown conformation with the lone pairs of the phosphine groups facing

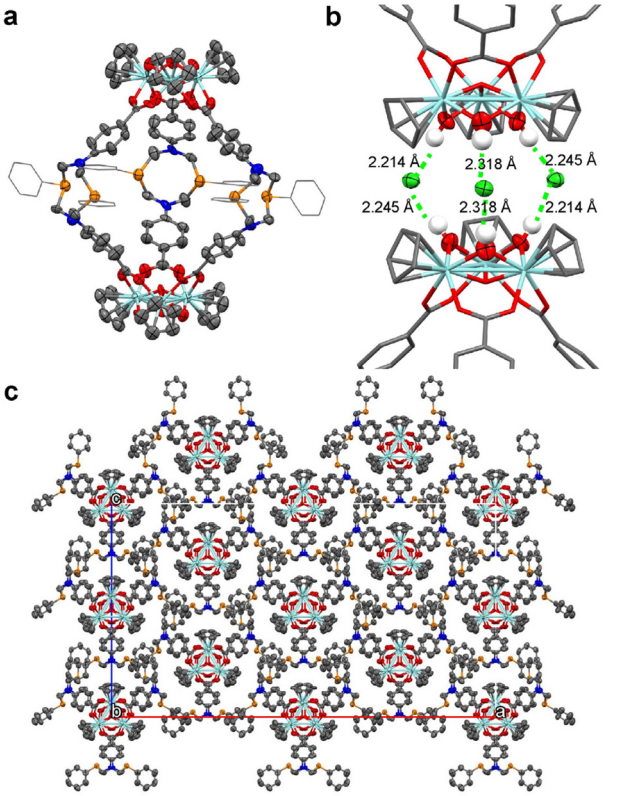

Fig. 1 (a) Molecular structure of **Zr–P_2N_2**. (b) Structure of adjacent Zr nodes showing hydrogen-bonding interactions between hydroxyl groups and chloride anions. (c) Packing of **Zr–P_2N_2** molecules (viewed along the *b*-axis). (Hydrogen atoms are omitted for clarity. Cyan: Zr, red: O, gray: C, green: Cl, orange: P, blue: N.)

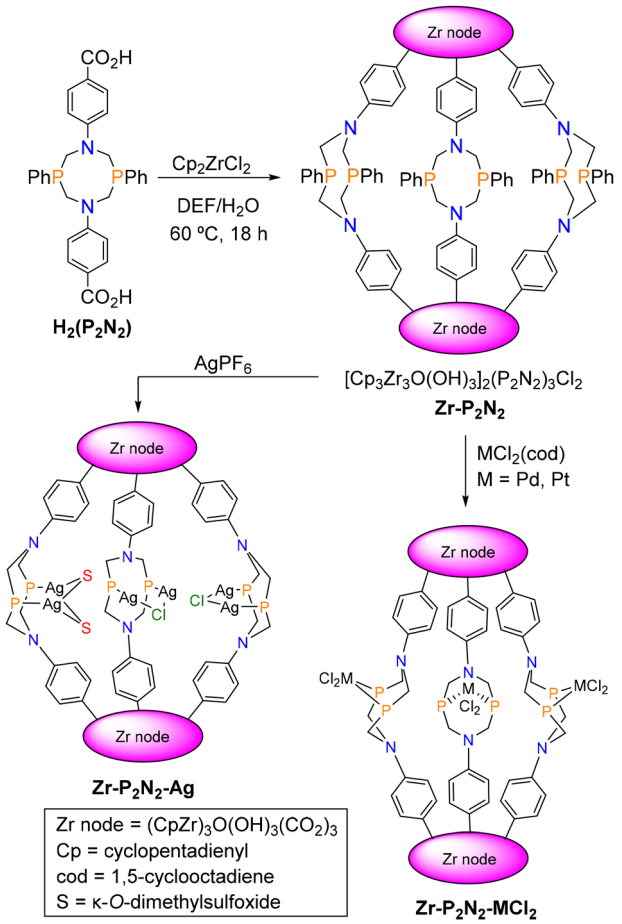

Scheme 2 Synthesis of **Zr–P_2N_2**, **Zr–P_2N_2–MCl_2**, and **Zr–P_2N_2–Ag**.

inward to the cage. Previous studies have shown that this is the most energetically favourable ligand conformation, and it is commonly observed in solid state structures of P_2N_2 ligands.[25] The sum of the bond angles around the N atoms (*ave*. 119.95°) reflects a nearly trigonal planar geometry arising from delocalization of the N lone pair into the aromatic ring of the benzoate group (Table S2). These features result in formation of a trigonal bipyramidal cage with a solvent-accessible cavity that is ~10 Å in diameter. Disordered DEF solvent molecules residing in the cage and interstitial space could not be adequately modelled in the structure refinement. The associated electron density was removed from the calculation using SQUEEZE (3715 electrons, 64 DEF molecules per unit cell).[26] The electron density map and ^{1}H NMR data indicate the presence of approximately one DEF molecule inside the cavity of each cage (Fig. S1).

The packing diagram of **Zr–P_2N_2** viewed along the *b*-axis shows a slipped-stacking arrangement with adjacent molecules displaced by approximately half a molecular length (Fig. 1c). Disordered chloride anions were located in pockets created by the μ-OH groups of the Zr clusters, supporting an empirical formula of $\{[Cp_3Zr_3O(OH)_3]_2(P_2N_2)_3\}Cl_2$ (Fig. 1b). Although the structure contains DEF solvent molecules in the interstitial space between the cages, **Zr–P_2N_2** does not retain permanent,

gas accessible porosity after desolvation, and N_2 adsorption isotherm measurements showed no measurable gas uptake. The absence of gas-accessible porosity in **Zr–P_2N_2** is consistent with other lantern-type Zr cages.[2]

Zr–P_2N_2 is slightly soluble in DMSO, EtOH and MeOH, but is insoluble in H_2O and most other polar organic solvents including DMF, acetone, and acetonitrile. The poor solubility of **Zr–P_2N_2** is at least partly attributed to strong hydrogen bonding interactions between the hydroxyl groups of the Zr clusters and the chloride counteranions. The ^{31}P NMR spectrum measured in DMSO-d_6 shows a single resonance at −40.9 ppm, which is shifted slightly downfield from the free linker (−47.4 ppm) (Fig. S2 and S3). The ^{1}H NMR spectrum exhibits all expected resonances for the η^5-Cp groups and $(P_2N_2)^{2-}$ linkers. The linker resonances experience very subtle changes in chemical shift compared to $H_2(P_2N_2)$. The μ-OH groups also appear as a sharp singlet at 9.76 ppm, supporting retention of the lantern cage structure in solution.[3] The ^{1}H DOSY NMR spectrum of **Zr–P_2N_2** in DMSO-d_6 shows an average diffusion coefficient of 7.98 × 10^{-11} m^2 s^{-1}, which is consistent with other reported lantern-type Zr MOCs (Fig. S4).[3,27]

ESI-MS data obtained for **Zr–P_2N_2** in MeOH solution show that the lantern cage structure is retained, but the phosphine groups undergo partial oxidation (Fig. S5). A mass signal corresponding to the parent cage (z = +2) is observed at m/z = 1346.04 and accompanied by a progression of minor species corresponding to sequential oxidation of the three diphosphine groups. The ^{31}P NMR spectrum of **Zr–P_2N_2** in MeOD-d_4 exhibits a single resonance at −43 ppm, even after exposure to ambient conditions for several days (Fig. S6). This result suggests that phosphine oxidation occurs *in situ* during the ESI-MS experiment rather than during sample preparation. Signals corresponding to the +1 ($-H^+$), +3 ($+H^+$), and +4 ($+2H^+$) forms of **Zr–P_2N_2** are also observed. Importantly, the isotopic distributions of these signals are consistent with the lantern-type structure, and no mass signals are observed in the m/z = 1789–1806 range, which would indicate the presence of a tetrahedral cage impurity with z = +3.

Synthesis and characterization of Zr–P_2N_2–MCl_2 (M = Pd, Pt)

The inward facing diphosphine groups of **Zr–P_2N_2** are not well poised to accommodate metal chelation. In addition to the small pore size (10 Å diameter, 589 $Å^3$ volume), the phosphine lone pairs diverge, precluding metal chelation without a significant distortion of the cage. Thus, we hypothesized that postsynthetic metalation would require either a linker flip such that the diphosphine groups point outward from the cage or restructuring to give a tetrahedral cage with more sterically accessible phosphine sites. Accordingly, suspensions of **Zr–P_2N_2** in MeOH were treated with 3 equiv. of $PdCl_2$(cod) (cod = η^4-1,5-cyclooctadiene) or $PtCl_2$(cod) and gently stirred for 16 h at room temperature. After isolation and washing, the solid products, **Zr–P_2N_2–$PdCl_2$** and **Zr–P_2N_2–$PtCl_2$**, were analysed by ^{31}P and ^{1}H NMR spectroscopy in DMSO-d_6. The ^{31}P NMR spectra showed a single resonance at +9.5 and −7.4 ppm for **Zr–P_2N_2–$PdCl_2$** and **Zr–P_2N_2–$PtCl_2$**, respectively (Fig. S7 and S8). The presence of a single, downfield shifted signal indicates formation of symmetric cages containing equivalent P_2N_2–MCl_2 metallolinkers (Fig. S9 and S10). The ^{1}H NMR spectra also exhibit signals consistent with symmetric, metalated linkers.

The postsynthetic metalation was further investigated by titrating **Zr–P_2N_2** solutions in DMSO-d_6 with up to 4 equiv. of MCl_2(cod) (M = Pd, Pt) and monitoring the reactions by ^{1}H and ^{31}P NMR spectroscopy (Fig. S11 and S12). Upon addition of 1–2 equiv. of the metal precursors, the ^{31}P NMR spectra show the appearance of product resonances at +10 ppm (**Zr–P_2N_2–$PdCl_2$**) and −6.8 ppm (**Zr–P_2N_2–$PtCl_2$**) with a concomitant decrease in the parent phosphine resonance at −41 ppm. The product signals appear abruptly and without the appearance of any discernible intermediate species.

We have been unable to obtain single crystals of **Zr–P_2N_2–$PdCl_2$** and **Zr–P_2N_2–$PtCl_2$** suitable for X-ray diffraction using the postsynthetic metalation approach. Consequently, **H_2(P_2N_2–$PdCl_2$)** and **H_2(P_2N_2–$PtCl_2$)** metallolinkers were prepared (Fig. S9 and S10) and used for direct assembly of **Zr–P_2N_2–$PdCl_2$** and **Zr–P_2N_2–$PtCl_2$**. The ^{31}P and ^{1}H NMR spectra of the products match those obtained from postsynthetic metalation reactions, supporting the formation of the same products in both cases (Fig. S13 and S14). The direct assembly gave single crystals suitable for X-ray diffraction, revealing formation of isostructural, lantern-shaped MOCs with P_2N_2–MCl_2 metallolinkers. As predicted, the linkers undergo a flip, resulting in square planar $PdCl_2$ and $PtCl_2$ diphosphine groups that point outward from the cage (Fig. 2, Tables S3 and S4, Fig. S15 and S16). The heterocyclic P_2N_2 rings adopt chair–boat conformations with two of the MCl_2 units pointed up and the third pointed downward with respect to the primary axis of the lantern cage.[25] The presence of a single resonance in the ^{31}P NMR spectra indicates that the metallolinkers are dynamic in solution, undergoing rapid exchange of the up/down orientations of the MCl_2 units. The change in conformation of the P_2N_2 linkers from crown-type in **Zr–P_2N_2** to chair–boat in the **Zr–P_2N_2–MCl_2** structures also has a pronounced effect on the

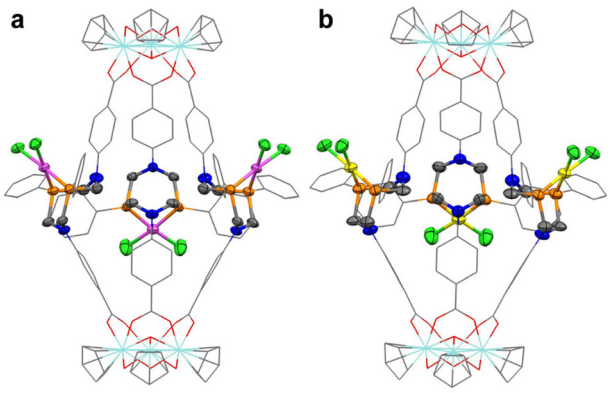

Fig. 2 Structures of (a) **Zr–P_2N_2–$PdCl_2$** and (b) **Zr–P_2N_2–$PtCl_2$**. (Hydrogen atoms are omitted for clarity. Cyan: Zr, red: O, gray: C, green: Cl, magenta: Pd, orange: P, blue: N, yellow: Pt.)

shape of the cages. The Zr···Zr distances between the metal nodes in **Zr–P_2N_2–MCl_2** (17.6 Å) are significantly longer than for the parent cage (15.1 Å) (Fig. S17). A concomitant decrease in the equatorial diameter diminishes the internal volume of the **Zr–P_2N_2–MCl_2** cages. Residual electron density in the interstitial spaces between the **Zr–P_2N_2–MCl_2** cages, attributed to disordered solvent molecules, was removed from the structure refinement using SQUEEZE. The calculation indicated 1839 electrons for **Zr–P_2N_2–$PdCl_2$** and 1596 electrons for **Zr–P_2N_2–$PtCl_2$** within the masks, corresponding to ~32 and ~28 DEF molecules per unit cell, respectively. The electron density maps suggest that no DEF molecules are present within the cavities of the cages, consistent with their decreased pore size compared to **Zr–P_2N_2**. Overall, the SCXRD data reveal significant structural changes, including a linker flip to generate outward facing Pd/Pt-diphosphine groups and a notable increase in the Zr···Zr intercluster distances.

The ^{1}H DOSY NMR spectra of **Zr–P_2N_2–MCl_2** in DMSO-d_6 show average diffusion coefficients of 8.89×10^{-11} m^2 s^{-1} for Pd and 8.61×10^{-11} m^2 s^{-1} for Pt (Fig. S18 and S19). These values are slightly larger than those of the parent **Zr–P_2N_2** (7.98×10^{-11} m^2 s^{-1}), indicating that the elongated structures of the **Zr–P_2N_2–MCl_2** cages reduces their effective hydrodynamic radius (Table S5).[27,28]

Zr–P_2N_2–$PdCl_2$ and **Zr–P_2N_2–$PtCl_2$** exhibit limited solubility in MeOH and DMSO and are insoluble in water and all other polar organic solvents tested. Moreover, the ^{1}H and ^{31}P NMR spectra measured in methanol-d_4 showed obvious decomposition, as indicated by the appearance of $PhPH_2$ (^{31}P: −124 ppm) and multiple new ^{1}H NMR resonances in the 6–9 ppm region (Fig. S20 and S21). This solvent sensitivity and limited solubility precluded characterization of the **Zr–P_2N_2–MCl_2** cages using ESI-MS. Attempts to improve their solubility *via* PF_6^-/Cl^- salt metathesis were largely unsuccessful due to increased solvent sensitivity (see SI for additional details). Consequently, **Zr–P_2N_2–$PdCl_2$** and **Zr–P_2N_2–$PtCl_2$** were analysed by MALDI-TOF mass spectrometry to verify that the lantern-type cage is maintained in bulk samples (Fig. S22 and S23). The MALDI spectrum of **Zr–P_2N_2–$PdCl_2$** displayed two mass signals (z = +2, 1612.29 amu and 1593.77 amu) that correspond to the parent lantern-type cage and the same ion with loss of an HCl equivalent from the Zr–OH and $PdCl_2$ groups. The MALDI spectrum of **Zr–P_2N_2–$PtCl_2$** showed only a single mass signal (z = +2, 1745.39 amu) associated with the parent ion. No trace signals corresponding to tetrahedral cages were observed for either sample. These results indicate that **Zr–P_2N_2–$PdCl_2$** and **Zr–P_2N_2–$PtCl_2$** exclusively form lantern-type cages, consistent with the structures determined by SCXRD.

Synthesis and characterization of Zr–P_2N_2–Ag

The solid-state structures of **Zr–P_2N_2–$PdCl_2$** and **Zr–P_2N_2–$PtCl_2$** raised the question of whether **Zr–P_2N_2** could accommodate metal coordination at the diphosphine groups in the cage interior without undergoing a linker flip. To test this possibility, we considered silver phosphine species which present a minimal steric profile. Accordingly, a suspension of **Zr–P_2N_2** in DMSO was treated with 6 equiv. of $AgPF_6$. Colourless crystals of **Zr–P_2N_2–Ag** suitable for X-ray diffraction were obtained by ethyl acetate vapor diffusion into the reaction solution. However, the structure solution and refinement were limited by weak diffraction and significant disorder of the guest solvent molecules and counteranions, resulting in high R-factors (R_1 = 0.2131, wR_2 = 0.5733, see SI for additional details). The resulting data preclude detailed analysis of bond metrics but establish connectivity of the core structure. **Zr–P_2N_2–Ag** adopts a lantern-type structure resembling the parent **Zr–P_2N_2** but with dinuclear Ag species complexed at each of the diphosphine ligands in the interior of the cage (Fig. 3,

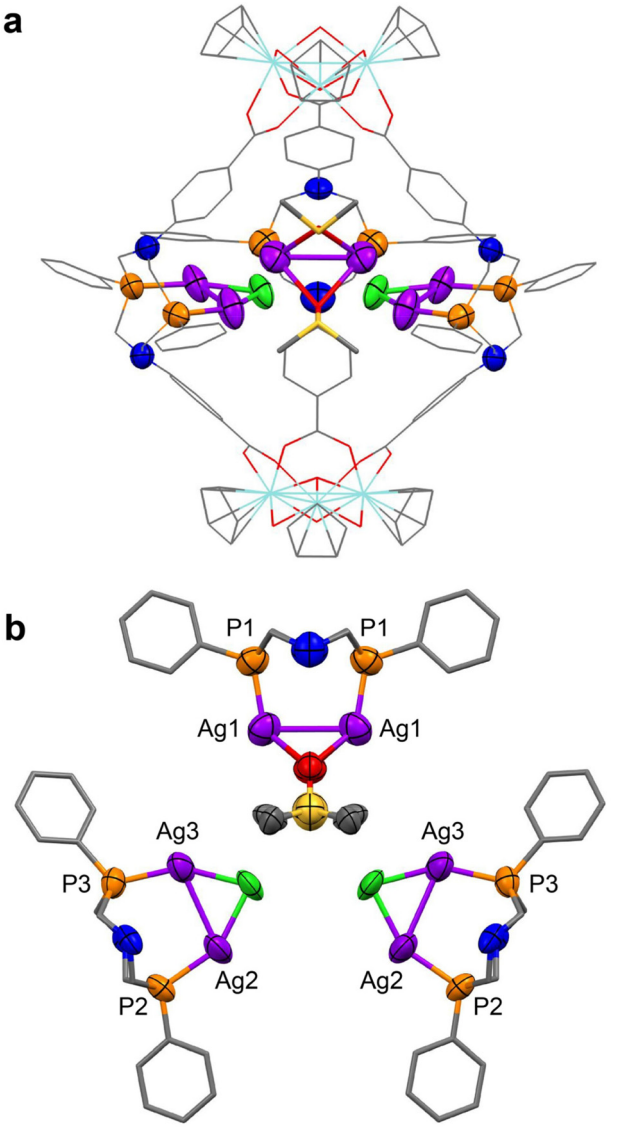

Fig. 3 (a) Molecular structure of the **Zr–P_2N_2–Ag** cage viewed along the equatorial plane and (b) truncated structure of the cage viewed down the axis containing the metal nodes. (Hydrogen atoms are omitted for clarity. Cyan: Zr, red: O, gray: C, green: Cl, purple: Ag, orange: P, blue: N, yellow: S.)

Fig. S30, and Tables S6 and S7). The cage is bisected by a mirror plane in the *Pbcm* space group, resulting in crystallographically inequivalent linkers. Two of the diphosphine ligands are equivalent and support unsymmetric, dinuclear species (Ag2 and Ag3) capped by a μ-Cl ligand originating from the **Zr–P_2N_2** counteranion. The remaining diphosphine ligand is bisected by the mirror plane and supports a symmetric dinuclear Ag species with two bridging κ-*O*-DMSO ligands. As a result, each Ag1 atom is three-coordinate and adopts a distorted Y-shaped geometry. The presence of two chloride ligands in the hexanuclear Ag core suggests that each **Zr–P_2N_2–Ag** molecule should bear an overall charge of +6, which is balanced by disordered PF_6^- or Cl^- ions residing outside of the cage.

The Zr⋯Zr distance between metal nodes in **Zr–P_2N_2–Ag** (*ave*. 15.7 Å) is comparable to that of the parent **Zr–P_2N_2** (15.1 Å), indicating that the cage does not require significant distortion to accommodate complexation of the Ag species. The preferential accumulation of the three Ag_2 units inside the cage appears to arise from a combination of steric and geometric factors inherent to the P_2N_2 ligands and the cage structure. The intraligand P⋯P distances are relatively short for the chelate species in **Zr–P_2N_2–MCl_2** (*ave*. 3.039 Å for Pd and 3.029 Å for Pt) and much longer for the dinucleating ligands in **Zr–P_2N_2–Ag** (*ave.* 3.912 Å) owing to the diverging metal–phosphine bond vectors. The different coordination modes affect the relative orientation of the phenyl substituents, which splay toward the P_2MCl_2 chelate groups in **Zr–P_2N_2–MCl_2** but bend away from the P_2Ag_2 units in **Zr–P_2N_2–Ag**. As a result, the inward-facing P_2Ag_2 groups alleviate unfavorable steric interactions that would occur if they were outward-facing.

Crystalline samples of **Zr–P_2N_2–Ag** were dissolved in DMSO-d_6 and analysed by ^{1}H and ^{31}P NMR spectroscopy. The ^{31}P NMR spectrum is consistent with the presence of the three crystallographically unique silver-phosphine sites observed in the solid-state structure (Fig. 3b). The three phosphine resonances centered around −19, −23, and −28 ppm each appear as two doublets owing to spin–spin coupling with ^{107}Ag (I = 1/2, ∼52% abundance) and ^{109}Ag (I = 1/2, ∼48% abundance) isotopes (Fig. 4). The ^{31}P NMR spectrum was also measured at a higher magnetic field strength to clearly resolve the individual signals and coupling constants of the isotopologues (Fig. S34). The $^1J(^{107}Ag–^{31}P)$ and $^1J(^{109}Ag–^{31}P)$ coupling constants were assigned based on the relative gyromagnetic ratios of the isotopes ($\gamma(^{109}Ag)/\gamma(^{107}Ag) \approx 1.15$).[29] The $^1J(^{107}Ag–^{31}P)$ (582–617 Hz) and $^1J(^{109}Ag–^{31}P)$ (676–710 Hz) values are comparable to those reported for other diphosphine bridged, dinuclear Ag complexes.[30,31] However, given the similarity in the Ag coordination environments and NMR chemical shifts, the resonances cannot be unambiguously assigned to the corresponding phosphine groups in the structure of **Zr–P_2N_2–Ag**. The ^{1}H NMR spectrum displays three Zr–OH group resonances and overlapping multiplets in both the aromatic and aliphatic regions, which is consistent with the lower symmetry of **Zr–P_2N_2–Ag** relative to the parent cage (Fig. S31). **Zr–P_2N_2–Ag** was also analyzed by mass spectrometry using MALDI-TOF and ESI-MS in acetonitrile solution (Fig. S35–S37). Both spectra show signals for z = +2 ions corresponding to the hexasilver parent cage with solvent exchange or adduct formation with the MALDI matrix. In addition, inductively-coupled plasma optical emission spectroscopy (ICP-OES) provided a Zr : Ag ratio of 1 : 0.98 which is consistent with the expected stoichiometry (6 Ag and 6 Zr per cage) for **Zr–P_2N_2–Ag** (Fig. S38).

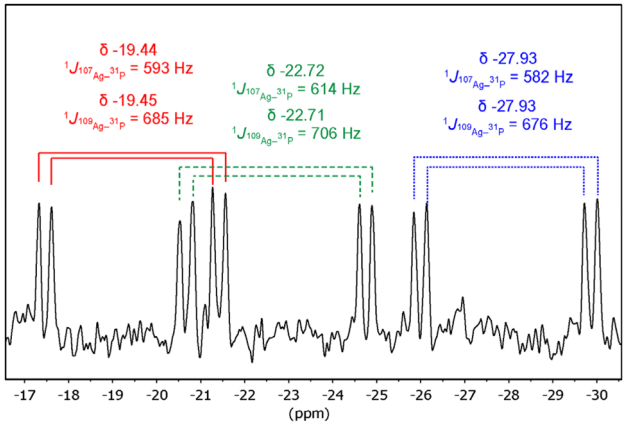

Fig. 4 $^{31}P\{^1H\}$ NMR spectrum of **Zr–P_2N_2–Ag** (DMSO-d_6, 162 MHz) showing the Ag–P coupling and chemical shifts of the doublets.

Conclusions

In summary, we report the synthesis and structural characterization of a new lantern-type MOC, **Zr–P_2N_2**, comprised of trinuclear Zr metal nodes and linkers based on the known P_2N_2 ligand motif. There are only two previously reported MOCs with phosphine-functionalized linkers, and both contain sterically accessible phosphine groups poised for metal coordination.[19,20] However, in **Zr–P_2N_2**, the diphosphine donor groups point into the small cavity of the lantern-type cage. The limited pore space and divergent phosphine lone pairs preclude diphosphine chelation of metal fragments inside the cage. Consequently, reaction of **Zr–P_2N_2** with MCl_2(cod) (M = Pd, Pt) induces a linker flip, resulting in outward-facing $(P_2N_2)PdCl_2$ and $(P_2N_2)PtCl_2$ groups. This adaptive behaviour points to dynamic linker exchange processes reminiscent of those observed for related Zr MOFs.[32,33] In contrast, metalation of **Zr–P_2N_2** with $AgPF_6$ affords a hexasilver cage, **Zr–P_2N_2–Ag**, with dinuclear Ag species complexed in the interior of the cage. Retention of the inward-facing diphosphine groups is enabled by the smaller steric profile of the dinuclear silver fragments along with the bridging, rather than chelating, mode of the diphosphine ligands. The adaptive structure of **Zr–P_2N_2** offers possibilities for designing switchable catalysts, sensors, or selective metal capture systems. Our ongoing efforts are focused on improving the solubility and stability of **Zr–P_2N_2** and related MOCs to further explore these applications.

Experimental

Materials and methods

Bis(hydroxymethyl)phenylphosphine, $PdCl_2$(cod), and $PtCl_2$(cod) were prepared following reported procedures.[34–36] 4-aminobenzoic acid (Alfa Aesar, 99%), *trans*-2-[3-(4-*tert*-butylphenyl)-2-methyl-2-propenylidene]malononitrile (DCTB, Fisher, 98+%), *N*,*N*-dimethylformamide (DMF, Fisher Chemical), *N*,*N*-diethylformamide (DEF, TCI America), acetone (Fisher Chemical), ethyl acetate (Fisher Chemical), and dimethyl sulfoxide (VWR Chemicals) were used as received. Cp_2ZrCl_2 (Thermo Scientific, 98%) was used as received and stored in a N_2-filled glovebox. Phenylphosphine (Beantown Chemical) and $AgPF_6$ (TCI America) were used as received and stored at −20 °C in a N_2-filled glovebox. All other solvents and reagents were of reagent grade and used as received.

Solution-state NMR spectra were collected using a Bruker DPX 400 or AVIII 600 MHz spectrometer. For ^{1}H NMR spectra, the solvent resonance was referenced as an internal standard. For $^{31}P\{^1H\}$ NMR spectra, 85% H_3PO_4 was used as an external standard (0 ppm). For ^{1}H DOSY NMR spectroscopy, saturated solutions of the analyte in DMSO-d_6 or MeOD-d_4 were analysed using a Bruker AVIII 600 MHz spectrometer. The μ-OH resonances were excluded for average diffusion coefficients (D) calculations due to their potential exchange with H_2O.

Single crystal X-ray diffraction analyses were performed using a Bruker Kappa Photon III Diffractometer equipped with Mo Kα radiation (λ = 0.71073 Å). Each crystal was mounted on a MiTeGen micromount with paratone oil. The analyses were conducted under N_2 flow at temperatures of 100 K or 240 K. The structures were solved using ShelXT and refined with SHELXL implemented in the Olex2 1.5 software package.[37–39]

ICP-OES analyses were performed using an Agilent 5100 ICP-OES spectrometer. **Zr–P_2N_2–Ag** samples were digested in a 3 : 1 (v/v) mixture of H_2SO_4 (ThermoSci, 99.999% metal-basis) and H_2O_2 (Ricca Chemical). Calibration curves were prepared using commercial ICP standards (Ag, VWR Chemicals; Zr, Inorganic Ventures). Powder X-ray diffraction patterns were collected using a Rigaku Miniflex 600 Diffractometer equipped with nickel-filtered Cu Kα radiation (λ = 1.5418 Å).

Mass spectrometry

Electrospray ionization (ESI) mass spectrometry data were collected with a ThermoFisher Orbitrap Exploris MX and Vanquish HPLC mass spectrometer. MALDI-TOF mass spectrometry data were collected using a Bruker Microflex LRF in reflection mode. Saturated solutions of analyte and matrix (DCTB) were prepared separately in 100 μL of DMSO. The solutions were then combined in an Eppendorf tube, and the resulting mixture was spotted onto a Bruker MSP 96 polished steel BC plate. After drying completely, the spots formed light yellow solids. ESI-MS and MALDI-TOF MS spectra were simulated using the molecular mass calculator and "Soup of Peaks" tools available *via* the open-access EPFL Mass Spectrometry Toolbox.[40]

Synthetic procedures

Synthesis of $H_2(P_2N_2)$. The linker was synthesized following a modified literature procedure.[24] In a N_2-filled glovebox, bis(hydroxymethyl)phenylphosphine (481 mg, 2.83 mmol), 4-aminobenzoic acid (388 mg, 2.83 mmol), and degassed ethanol (20 mL) were charged in a 35 mL CEM microwave vessel with a Teflon stir bar. The tube was sealed and heated at 100 °C for 18 hours in a CEM Discover SP microwave reactor. Following the reaction, the vessel was cooled in a −4 °C freezer for 15 min. The resulting white precipitate was collected *via* vacuum-filtration and washed with cold ethanol (5 × 10 mL). The solid was dried *in vacuo* and characterized *via* ^{1}H and $^{31}P\{^1H\}$ NMR spectroscopy. Yield: 710 mg (93%). ^{1}H NMR (600 MHz, DMSO-d_6): δ 12.08 (s, 2H, –COOH), 7.75–7.72 (m, 8H, Ar), 7.55–7.49 (m, 6H, Ar), 6.75 (d, 4H, Ar), 4.65 (dd, $^2J_{H-H}$ = 15.2, $^2J_{H-P}$ = 5.7 Hz, 4H, alkyl), 4.22 (d, $^2J_{H-H}$ = 14.1 Hz, 4H, alkyl). $^{31}P\{^1H\}$ NMR (162 MHz, DMSO-d_6): δ −47.44 (s).

Synthesis of Zr–P_2N_2. A 20 mL scintillation vial was charged with $H_2(P_2N_2)$ (50 mg, 0.092 mmol), Cp_2ZrCl_2 (54.0 mg, 0.185 mmol), H_2O (0.3 mL), and DEF (3 mL) and sealed with a Teflon-lined screw cap. The mixture was sonicated for 10 min, resulting in a pale yellow suspension. The vial was placed in a room temperature oven and heated to 60 °C at a ramp rate of 10 °C h^{-1}. After 16 hours, the vial was slowly cooled to room temperature at a ramp rate of 15 °C/hr. The resulting white crystalline solid was collected *via* vacuum filtration and washed with DMF (5 × 5 mL) and acetone (5 × 5 mL). The solid was dried *in vacuo* and characterized *via* ^{1}H and $^{31}P\{^1H\}$ NMR spectroscopy. Yield: 44 mg (51.9%). For SCXRD data collection, the colourless block-like crystals were isolated without washing. ^{1}H NMR (400 MHz, DMSO-d_6): δ 9.76 (s, 2H, –OH), 7.83–7.76 (m, 8H, Ar), 7.59–7.58 (m, 6H, Ar), 6.68 (d, $^2J_{H-H}$ = 9.0 Hz, 4H, Ar), 6.41 (s, 10H, Cp), 4.69 (d, $^2J_{H-H}$ = 15.7 Hz, 4H, alkyl), 4.33–4.27 (m, 4H, alkyl). $^{31}P\{^1H\}$ NMR (162 MHz, DMSO-d_6): δ −40.89 (s). See SI for mass spectrometry data.

Direct synthesis of Zr–P_2N_2–$PdCl_2$. The $H_2(P_2N_2$–$PdCl_2)$ metallolinker was prepared *in situ* by dissolving $H_2(P_2N_2)$ (25 mg, 0.046 mmol) and $PdCl_2$(cod) (13 mg, 0.046 mmol) in DEF (9 mL) and H_2O (0.9 mL) in a 20 mL scintillation vial. Solid Cp_2ZrCl_2 (27 mg, 0.092 mmol) was added to the light yellow $H_2(P_2N_2$–$PdCl_2)$ solution. The vial was sealed with a Teflon-lined screw cap and sonicated for 5 min resulting in a yellow solution. The vial was placed in a room temperature oven and heated to 60 °C at a ramp rate of 10 °C h^{-1}. After 18 hours, the vial was slowly cooled to room temperature at a ramp rate of 15 °C h^{-1}. The resulting yellow plate-like crystals were washed with acetone (5 mL) and characterized by ^{1}H and $^{31}P\{^1H\}$ NMR spectroscopy and SCXRD. Yield: 20 mg (41%). ^{1}H NMR (600 MHz, DMSO-d_6) δ 10.08 (s, 2H), 7.84–7.83 (m, 4H), 7.78 (d, $^2J_{H-H}$ = 8.9 Hz, 4H), 7.72–7.70 (m, 2H), 7.67–7.65 (m, 4H), 6.99 (d, $^2J_{H-H}$ = 8.3 Hz, 4H), 6.55 (s, 10H), 4.75 (d, J = 14.6 Hz, 4H), 4.15 (s, 4H). $^{31}P\{^1H\}$ NMR (243 MHz, DMSO-d_6) δ 9.94. See SI for mass spectrometry data.

Direct synthesis of Zr–P_2N_2–$PtCl_2$. The $H_2(P_2N_2$–$PtCl_2)$ metallolinker was prepared *in situ* by dissolving $H_2(P_2N_2)$ (25 mg,

0.046 mmol) and $PtCl_2$(cod) (17 mg, 0.046 mmol) in DEF (9 mL) and H_2O (0.9 mL) in a 20 mL scintillation vial. The mixture was stirred and heated at 50 °C for 16 h. Solid Cp_2ZrCl_2 (27 mg, 0.092 mmol) was added to the light yellow $H_2(P_2N_2–PtCl_2)$ solution. The vial sealed with a Teflon-lined screw cap and sonicated for 5 min resulting in a yellow solution. The vial was placed in a room temperature oven and heated to 60 °C at a ramp rate of 10 °C h^{-1}. After 18 hours, the vial was slowly cooled to room temperature at a ramp rate of 15 °C h^{-1}. The resulting colourless plate-like crystals were washed with acetone (5 mL) and characterized by ^1H and $^{31}P\{^1H\}$ NMR spectroscopy and SCXRD. Yield: 34 mg (63%) ^1H NMR (600 MHz, DMSO-d_6) δ 10.08 (s, 2H), 7.84–7.82 (m, 4H), 7.78 (d, $^2J_{H–H}$ = 8.6 Hz, 4H), 7.69–7.67 (m, 6H), 6.99 (d, $^2J_{H–H}$ = 8.8 Hz, 4H), 6.55 (s, 10H), 4.67 (d, J = 15.4 Hz, 4H), 4.31 (s, 4H). $^{31}P\{^1H\}$ NMR (243 MHz, DMSO-d_6) δ −6.84. See SI for mass spectrometry data.

Synthesis of Zr–P_2N_2–Ag. **Zr–P_2N_2** (0.018 mmol) was suspended in DMSO (2 mL). A solution of $AgPF_6$ (27 mg, 0.108 mmol) in DMSO (0.5 mL) was added to the **Zr–P_2N_2** suspension, resulting in a pale-yellow solution and some colourless solids. The reaction was filtered using a PTFE syringe filter (0.45 μm), and the filtrate was subjected to vapor diffusion of ethyl acetate. After one month, colourless block-like crystals were obtained and analyzed *via* SCXRD. Rapid addition of EtOAc (20 mL) to the filtrate resulted in precipitation of the product as a colorless powder. The powder was collected *via* centrifugation and washed with ethyl acetate. Yield: 32 mg (44.4%). ^1H NMR (600 MHz, DMSO-d_6) δ 10.03–9.91 (m, 2H), 7.95–7.75 (m, 13H), 6.76–6.71 (m, 3H), 6.59–6.57 (m, 1H), 6.43–6.37 (m, 10H), 5.22 (s, 3H), 5.03 (m, 1H), 4.78–4.63 (m, 3H), 4.35 (s, 1H). $^{31}P\{^1H\}$ NMR (162 MHz, DMSO-d_6) −19.44 (d, $^1J_{Ag–P}$ = 593 Hz), −19.45 (d, $^1J_{Ag–P}$ = 685 Hz), −22.72 (d, $^1J_{Ag–P}$ = 614 Hz), −22.71 (d, $^1J_{Ag–P}$ = 706 Hz), −27.93 (d, $^1J_{Ag–P}$ = 582 Hz), −27.93 (d, $^1J_{Ag–P}$ = 676 Hz). See SI for mass spectrometry data.

NMR titration procedures

NMR titration of Zr–P_2N_2 with MCl_2(cod) (M = Pd, Pt). **Zr–P_2N_2** (0.0018 mmol) was suspended in DMSO-d_6 (0.4 mL) and transferred to an NMR tube. ^1H and $^{31}P\{^1H\}$ NMR spectra were collected. A 0.05 M solution of MCl_2(cod) was prepared in DMSO-d_6 (3 mL). The NMR tube containing **Zr–P_2N_2** was titrated with aliquots of the 0.05 M MCl_2(cod) solutions in increments of 0.036 mL (*i.e.* 1 equiv. of M per **Zr–P_2N_2**). After each addition, the sample was analysed *via* ^1H and $^{31}P\{^1H\}$ NMR spectroscopy. The reaction was analyzed up to a total of 4 equiv. of MCl_2(cod). The **Zr–P_2N_2** suspension became a yellow solution upon addition of the MCl_2(cod) solution.

NMR titration of Zr–P_2N_2 with $AgPF_6$. **Zr–P_2N_2** (0.0018 mmol) was suspended in DMSO-d_6 (0.4 mL) and transferred to an NMR tube. ^1H and $^{31}P\{^1H\}$ NMR spectra were collected. A 0.05 M $AgPF_6$ solution was prepared by dissolving $AgPF_6$ (38 mg) in DMSO-d_6 (3 mL). The NMR tube containing **Zr–P_2N_2** was titrated with aliquots of the 0.05 M $AgPF_6$ solution in increments of 0.036 mL (*i.e.* 1 equiv. of Ag per **Zr–P_2N_2**). After each addition, the sample was analysed by ^1H and $^{31}P\{^1H\}$ NMR spectroscopy. The reaction was analysed up to a total of 6 equiv. of $AgPF_6$. The **Zr–P_2N_2** suspension became a yellow solution upon addition of the $AgPF_6$ solution.

Author contributions

J. S.: investigation, formal analysis, writing; C. R. W.: conceptualization, formal analysis, supervision, writing.

Conflicts of interest

There are no conflicts to declare.

Data availability

The data supporting this article have been included as part of the supplementary information (SI). Supplementary information: NMR spectral data, mass spectrometry data, crystallographic data, PXRD data, ICP-OES data, additional experimental details. See DOI: https://doi.org/10.1039/d6dt00536e.

CCDC 2535025–2535029 (**Zr–P_2N_2**, **Zr–P_2N_2–$PdCl_2$**, **Zr–P_2N_2–$PtCl_2$**, **Zr–P_2N_2–Ag** (masked counteranions) and **Zr–P_2N_2–Ag**) contain the supplementary crystallographic data for this paper.[41a–e]

Acknowledgements

This research was supported by the U.S. National Science Foundation under Grant No. CHE-2044904. We acknowledge resources from the Campus Chemical Instrumentation Center Nuclear Magnetic Resonance Facility and Mass Spectrometry and Proteomics Facility at The Ohio State University. These facilities are supported in part by funding from OSU's Enterprise for Research, Innovation and Knowledge.

References

1 S. Lee, J. H. Lee, J. C. Kim, S. Lee, S. K. Kwak and W. Choe, *ACS Appl. Mater. Interfaces*, 2018, **10**, 8685–8691.
2 A. J. Gosselin, G. E. Decker, B. W. McNichols, J. E. Baumann, G. P. A. Yap, A. Sellinger and E. D. Bloch, *Chem. Mater.*, 2020, **32**, 5872–5878.
3 M. G. Sullivan, H. K. Welgama, M. R. Crawley, A. E. Friedman and T. R. Cook, *Chem. Mater.*, 2024, **36**, 567–574.
4 B. S. Pilgrim and N. R. Champness, *ChemPlusChem*, 2020, **85**, 1842–1856.
5 E.-S. M. El-Sayed, Y. Di Yuan, D. Zhao and D. Yuan, *Acc. Chem. Res.*, 2022, **55**, 1546–1560.

6 C. García-Simón, R. Gramage-Doria, S. Raoufmoghaddam, T. Parella, M. Costas, X. Ribas and J. N. H. Reek, *J. Am. Chem. Soc.*, 2015, **137**, 2680–2687.
7 S. Chen, K. Li, F. Zhao, L. Zhang, M. Pan, Y.-Z. Fan, J. Guo, J. Shi and C.-Y. Su, *Nat. Commun.*, 2016, **7**, 13169.
8 J. Guo, Y. Xu, K. Li, L. Xiao, S. Chen, K. Wu, X. Chen, Y. Fan, J. Liu and C. Su, *Angew. Chem., Int. Ed.*, 2017, **56**, 3852–3856.
9 J. Jiao, C. Tan, Z. Li, Y. Liu, X. Han and Y. Cui, *J. Am. Chem. Soc.*, 2018, **140**, 2251–2259.
10 M. T. Yong, O. M. Linder-Patton and W. M. Bloch, *Inorg. Chem.*, 2022, **61**, 12863–12869.
11 G. Liu, M. Zeller, K. Su, J. Pang, Z. Ju, D. Yuan and M. Hong, *Chem. – Eur. J.*, 2016, **22**, 17345–17350.
12 H. S. Lee, S. Jee, R. Kim, H.-T. Bui, B. Kim, J.-K. Kim, K. S. Park, W. Choi, W. Kim and K. M. Choi, *Energy Environ. Sci.*, 2020, **13**, 519–526.
13 C. Ji, W. Wang, E.-S. M. El-Sayed, G. Liu, Y. Si, K. Su, Z. Ju, F. Wu and D. Yuan, *Appl. Catal., B*, 2021, **285**, 119782.
14 S. Kim, S. Jee, K. M. Choi and D.-S. Shin, *Nano Res.*, 2021, **14**, 486–492.
15 C. A. Tolman, *Chem. Rev.*, 1977, **77**, 313–348.
16 M. L. Clarke and J. J. R. Frew, in *Organometallic Chemistry*, ed. I. J. S. Fairlamb and J. M. Lynam, Royal Society of Chemistry, Cambridge, 2009, vol. 35, pp. 19–46.
17 D. Setiawan, R. Kalescky, E. Kraka and D. Cremer, *Inorg. Chem.*, 2016, **55**, 2332–2344.
18 W. Chen, P. Cai, H. Zhou and S. T. Madrahimov, *Angew. Chem., Int. Ed.*, 2024, **63**, e202315075.
19 C. T. McTernan, T. K. Ronson and J. R. Nitschke, *J. Am. Chem. Soc.*, 2019, **141**, 6837–6842.
20 X. Zhao, M. Sun, Y. Li, H. Jiang, Y. Cui and Y. Liu, *J. Am. Chem. Soc.*, 2026, **148**, 1141–1152.
21 E. S. Wiedner, A. M. Appel, S. Raugei, W. J. Shaw and R. M. Bullock, *Chem. Rev.*, 2022, **122**, 12427–12474.
22 Z. Chen, E. S. Isbrandt and S. G. Newman, *Org. Lett.*, 2024, **26**, 7723–7727.
23 E. S. Isbrandt, D. E. Chapple, N. T. P. Tu, V. Dimakos, A. M. M. Beardall, P. D. Boyle, C. N. Rowley, J. M. Blacquiere and S. G. Newman, *J. Am. Chem. Soc.*, 2024, **146**, 5650–5660.
24 G. N. Nikonov, A. S. Balueva, O. A. Erastov and B. A. Arbuzov, *Bull. Acad. Sci. USSR, Div. Chem. Sci.*, 1989, **38**, 1223–1226.
25 S. Latypov, A. Strelnik, A. Balueva, Y. Spiridonova, A. Karasik and O. Sinyashin, *Eur. J. Inorg. Chem.*, 2016, **2016**, 1068–1084.
26 A. L. Spek, *Acta Crystallogr., Sect. C: Struct. Chem.*, 2015, **71**, 9–18.
27 G. A. Taggart, A. Guliyeva, K. Kim, G. P. A. Yap, D. J. Pochan, T. H. Epps and E. D. Bloch, *J. Phys. Chem. C*, 2023, **127**, 2379–2386.
28 P. Groves, *Polym. Chem.*, 2017, **8**, 6700–6708.
29 C.-W. Burges, R. Koschmieder, W. Sahm and A. Schwenk, *Z. Naturforsch., A*, 1973, **28**, 1753–1758.
30 M. Ohkouchi, D. Masui, M. Yamaguchi and T. Yamagishi, *J. Mol. Catal. A: Chem.*, 2001, **170**, 1–15.
31 K. Plevová, L. J. Prieto Pabon, M. Gaysinski, S. Poulain-Martini and V. Michelet, *ChemPlusChem*, 2022, **87**, e202200217.
32 M. Kim, J. F. Cahill, Y. Su, K. A. Prather and S. M. Cohen, *Chem. Sci.*, 2012, **3**, 126–130.
33 L. Feng, G. S. Day, K.-Y. Wang, S. Yuan and H.-C. Zhou, *Chem*, 2020, **6**, 2902–2923.
34 K. Peng, V. Mawamba, E. Schulz, M. Löhr, C. Hagemann and U. Schatzschneider, *Inorg. Chem.*, 2019, **58**, 11508–11521.
35 C. Janot, J.-B. Chagnoleau, N. R. Halcovitch, J. Muir and C. Aïssa, *J. Org. Chem.*, 2020, **85**, 1126–1137.
36 A. F. Greene, J. Shin and C. R. Wade, *Organometallics*, 2024, **43**, 2434–2442.
37 O. V. Dolomanov, L. J. Bourhis, R. J. Gildea, J. A. K. Howard and H. Puschmann, *J. Appl. Crystallogr.*, 2009, **42**, 339–341.
38 G. M. Sheldrick, *Acta Crystallogr., Sect. C:Struct. Chem.*, 2015, **71**, 3–8.
39 G. M. Sheldrick, *Acta Crystallogr., Sect. A:Found. Adv.*, 2015, **71**, 3–8.
40 MS ToolS (EPFL). Online Mass Spectrometry Tools – EPFL MSToolbox. https://ms.epfl.ch/ (accessed 2024–2025).
41 (*a*) CCDC 2535025: Experimental Crystal Structure Determination, 2026, DOI: 10.5517/ccdc.csd.cc2r2x0s; (*b*) CCDC 2535026: Experimental Crystal Structure Determination, 2026, DOI: 10.5517/ccdc.csd.cc2r2x1t; (*c*) CCDC 2535027: Experimental Crystal Structure Determination, 2026, DOI: 10.5517/ccdc.csd.cc2r2x2v; (*d*) CCDC 2535028: Experimental Crystal Structure Determination, 2026, DOI: 10.5517/ccdc.csd.cc2r2x3w; (*e*) CCDC 2535029: Experimental Crystal Structure Determination, 2026, DOI: 10.5517/ccdc.csd.cc2r2x4x.